Nanoindentation cannot accurately predict the tensile strength of graphene or other 2D materials

Jihoon Han[a,b], Nicola M. Pugno[c,d,e] and Seunghwa Ryu[*a]

[a] Department of Mechanical Engineering, Korea Advanced Institute of Science and Technology (KAIST), 291 Daehak-ro, Yuseong-gu, Daejeon, 305-701, Republic of Korea. E-mail: ryush@kaist.ac.kr

[b] Research Reactor Utilization Department, Korea Atomic Energy Research Institute, 898-111 Daedeok-daero, Yuseong-gu, Daejeon, 305-535, Republic of Korea

[c] Laboratory of Bio-Inspired and Graphene Nanomechanics, Department of Civil, Environmental and Mechanical Engineering, University of Trento, Via Mesiano 77, I-38123 Trento, Italy

[d] Centre for Materials and Microsystems, Fondazione Bruno Kessler, Via Sommarive 18, I-38123 Povo (Trento), Italy

[e] School of Engineering and Materials Science, Queen Mary University of London, Mile End Road, E1 4NS London, UK

Abstract

Due to the difficulty of performing uniaxial tensile testing, the strengths of graphene and its grain boundaries have been measured in experiments by nanoindentation testing. From a series of molecular dynamics simulations, we find that the strength measured in uniaxial simulation and the strength estimated from the nanoindentation fracture force can differ significantly. Fracture in tensile loading occurs simultaneously with the onset of crack nucleation near 5–7 defects, while the graphene sheets often sustain the indentation loads after the crack initiation because the sharply concentrated stress near the tip does not give rise to enough driving force for further crack propagation. Due to the concentrated stress, strength estimation is sensitive to the indenter tip position along the grain boundaries. Also, it approaches the strength of pristine graphene if the tip is located slightly away from the grain boundary line. Our findings reveal the limitations of nanoindentation testing in quantifying the strength of graphene, and show that the loading-mode-specific failure mechanism must be taken into account in designing reliable devices from graphene and other technologically important 2D materials.

Introduction

Pristine, defect-free graphene, which is packed in a honeycomb lattice with sp2 carbon–carbon bonds, exhibits exceptional mechanical properties,[1–4] showing great promise for the development of high strength materials and devices. The ideal intrinsic strength of 120 GPa and the in-plane stiffness of 1.0 TPa are mechanically measured by atomic-force-microscopybased nanoindentation testing for freely suspended pristine graphene prepared by mechanical exfoliation.[2,5–7] However, polycrystalline graphene synthesized by chemical vapor deposition[8–12] is an inevitable choice for realistic applications in need of large-area graphene. Recent transmission electron microscopy experiments[13–15] revealed that the grain boundary (GB) lines[16] consist of an array of pentagon–heptagon (5–7) defects and vacancies,[17–21] which can serve as stress-intensifying sites under mechanical loading.

To quantify the effect of GBs on the strength of polycrystalline graphene many theoretical and experimental studies have been performed using uniaxial tensile loading and nanoindentation testing.[22–32] In atomistic simulations, uniaxial tension simulations predict that the strength of polycrystalline graphene, even if only topological 5–7 defects without vacancies are considered, is lower than the strength of pristine graphene.[23–28] The weakening of polycrystalline graphene is

attributed to the buildup of pre-stress around 5–7 defects along GBs. In general, high-angle GBs show higher strength than low-angle GBs due to denser 5–7 defect pile-up, which counterbalances the dipole stress field more effectively.

Meanwhile, in experimental studies, strength levels determined in nanoindentation testing have only been reported due to the difficulty of performing uniaxial testing.[29–32] Lee et al.[32] reported that the GB strength is comparable to the strength of pristine graphene regardless of the misorientation angle, which is inconsistent with the theoretical predictions. In contrast, other studies[29–31] have shown that the strength of GB is significantly lower than the pristine strength, and that a GB with a higher angle has higher strength. To reveal the cause of the inconsistency between theoretical and experimental studies, as well as the mismatch among experimental nanoindentation testing, it is necessary to reveal the failure mechanism of graphene under different loadings. A few molecular dynamics simulation studies have reported the effect of defects on the failure force of nanoindentation[33,34] which is found to critically depend on the indentation site. Sha et al.[34] show that the fracture behaviour of polycrystalline graphene with GB triple junctions, which are regarded as the weakest points, in nanoindentation is critically dependent on the indentation site due to non-uniform stress distribution. For the strength of polycrystalline graphene, several molecular dynamics simulations are performed to investigate the effects of the grain size[38] and Stone–Thrower–Wales (STW) defects.[39] They revealed that the strength depends on the grain size under uniaxial tensile loading and follows an inverse pseudo Hall–Petch relationship. In another work, the strength of the STW defective graphene is dependent on defect orientation and tilting angles. However, a detailed investigation on the failure mechanism difference between the nanoindentation and the uniaxial tensile loading was missing, which can provide additional insight on the discrepancy.

In this study, we perform molecular dynamics simulations to compare the predicted strength as well as the failure mechanism in both uniaxial tensile and nanoindentation simulations. We limit the focus of our study on the bicrystal graphene to study the strength estimation of individual GBs in detail, and to mimic the typical experimental conditions where the indenter radius is much smaller than the grain size.[29–32] We find that fractures occur in tension simultaneously with the onset of crack nucleation near 5–7 defects. Under tensile loads, a uniform stress field is applied to the entire graphene sheet, providing a driving force for the catastrophic propagation of crack after crack nucleation. On the contrary, graphene sheets often sustain loads after crack nucleation during indentation simulations. The applied stress from nanoindentation is concentrated sharply around the indenter tip, and crack propagation does not follow crack nucleation immediately when the distance between 5–7 defects is large, i.e. in the case of low-angle GBs. Thus, the failure force from nanoindentation cannot be directly linked to the onset of crack nucleation.

Due to this stress concentration of the nanoindenter probe, strength estimation depends significantly on the indenter position along the GB. For the same reason, the predicted strengths of tilt GBs approach the strength of pristine graphene if the center of the indenter tip is located slightly away from the GB line. Our findings show the limitation of nanoindentation testing in quantifying the strength of graphene, and also imply that the loading-mode-specific failure mechanism must be taken into account in designing reliable devices from graphene and other technologically important 2D materials.

Methods

Here, we explain the methodology for nanoindentation simulation of graphene sheets. To calculate the tip force of indentation as a function of the indentation depth nanoindentation simulations are carried out at room temperature using molecular dynamics simulations. The simulation cell sizes are chosen to be around 50 nm × 50 nm along the x and y axes, and are sufficiently larger than stress fields of dislocation. The adaptive intermolecular reactive empirical bond order (AIREBO) potential[35]

is used to describe the bond interactions between carbon atoms in the graphene sheet. The cutoff radius of rcc = 1.92 Å (ref. 23, 24, 26 and 27) is used to avoid the influence of nonphysical behavior on the fracture process. Molecular dynamics simulations are performed using LAMMPS36 with a time step of 1.0 fs. The samples are initially equilibrated for 20 ps, using the NPT ensemble (widely known as isothermal–isobaric ensemble) at 300 K. Nanoindentation simulation is conducted with an NVT ensemble (widely known as Nosé–Hoover thermostat) at 300 K.

We consider a frictionless rigid spherical indenter of radius R that exerts a force on each atom given by:

$$F(r) = -K(r - R)^2 \qquad (1)$$

where K, r, and R indicate the specific force constant, the distance from each atom to the center of the indenter, and the radius of the spherical indenter, respectively. The non-zero value of the repulsive force exerts for r < R. In our study, a K value of 10 eV Å−3 and an R value of 50 Å are used to simulate the indentation of the polycrystalline graphene. Note that the ratio of indenter radius to sample size (R/L ≈ 1/5) is similar to that used in Rasool's experimental conditions.30 It has been shown that the rupture force does not depend on the sample size if it is more than twice larger than the indenter radius.40

The carbon atoms inside the circular hole region could freely move (blue atoms in Fig. 1(a)), but the atoms outside the circular hole region are fixed to form a clamped boundary condition (red atoms in Fig. 1(a)). The position of the indenter tip is located on the geometric center of the polycrystalline graphene and is moved in the z-direction by 0.1 Å from the original position of the indenter at every 5 ps until it fails completely. A constant indenter speed of 0.02 Å ps−1 is used (see section S2 of the ESI for the effect of indenter speed). As the indenter gradually moves downward, the force exerted on the indenter is measured for the circular clamped graphene sheet. The force is averaged over 5 ps at each deformation increment to average out thermal fluctuation.

Results and discussion

We first perform nanoindentation of a pristine graphene sheet via molecular dynamics simulations, as shown in Fig. 1(a). We obtain the force–deflection curve for pristine graphene, as depicted in Fig. 1(b). Fig. 1(c) presents the sharp stress concentration around the indenter tip on the verge of rupture (see Fig. S4 in the ESI† for the stress field on the graphene sheets with and without GB). The atomic virial stress is calculated with an atomic volume of 8.8 Å3 . 24 Combining Fig. 1(b) and (c) at various indentation depths, we obtain the indenter tip stress versus force curve for pristine graphene, as shown in Fig. 1(d). Indenter stresses are defined by the average maximum stress between σxx and σyy at various indentation depths. In the remaining part of this study, following previous studies, we estimate the strength of polycrystalline graphene by converting the failure force into the strength using the stress–force relationship (see Fig. 1(d)).2,30,32 Thus, GB strengths, which are estimated by the failure force, are directly compared with the strength measured by tensile simulations.

The estimated strength of pristine graphene is 105 GPa, which is in good agreement with the results of the experimental nanoindentation tests.2,30,32 In comparison, the previous uniaxial tension simulations, conducted using the same empirical potential, predict a strength of 120 GPa.23,26,27 The strength is underestimated in the nanoindentation test because the graphene sheet is subjected to equibiaxial tensile load. The strength obtained from biaxial tensile simulation shows a good match with the strength estimated from nanoindentation (see Fig. S3 in the ESI). Basically, crack nucleates when the maximum stress reaches the materials strength. In addition, we carefully compare the failure mechanism between the uniaxial tensile simulation and the nanoindentation simulation. Both studies predict catastrophic crack propagation right after the crack initiation (see Fig. 2). This implies that both tests capture the onset of crack nucleation, and thus can serve as equivalent tests for

estimating the graphene strength, apart from the different strength estimation values that originate from the different stress states.

Having established the validity of the nanoindentation simulation for pristine graphene, we carry out nanoindentation simulations for bi-crystalline graphene sheets having GBs with various misorientation tilt angles. We construct a series of symmetric and asymmetric tilt GBs with various tilt angles (see Fig. S1 in the ESI†). We place the GB line at the center of the hole and measure the failure force as a function of the indenter location along the GB line (see the inset of Fig. 3(a)). The 5–7 defects are periodically located for the symmetric tilt GBs, and the distance between 5–7 defects increases with the decreasing tilt angle. The inter-defect distance is 40 Å for symmetric tilt GB with an angle of 5.7°, and 8 Å for symmetric tilt GB with an angle of 27.8°. Interestingly, the failure force turns out to be sensitive to the location of the indenter for low angle tilt GBs. The failure force can be converted to the strength estimation via the stress–force plot, as shown in Fig. 1(d). We plot the strength estimation as a function of distance (D), where D = 0 refers to the center of the 5–7 defect. The entire graphene sheet is shifted by distance D when the distance between the indenter tip and the 5–7 defect is adjusted. The strength estimation can vary up to 50%, and this is significantly beyond the statistical error from thermal fluctuations, as shown in Fig. 3(a). We perform an equivalent set of simulations for asymmetric tilt GBs, and obtain similar results, as shown in Fig. 3(b). All stress–strain curves are depicted in Fig. S6 and S7 in the ESI.

For various tilt angles, the estimated strengths from the failure force of nanoindentation are compared with the strengths obtained from uniaxial tensile simulations, as shown in Fig. 3(c) and (d). We present the strength minima and maxima from Fig. 3(a) and (b) as error bars, which show a wide scatter for the same tilt angle. Such a wide range of strength estimation for the same tilt angle has also been observed in the previous nanoindentation experiments.[30] Given that a wide range of strength estimation can be obtained for the same GB configuration, even wider strength estimation is expected in experiments in which many different GB configurations are found for a similar tilt angle. Notably, the strength of GB is overestimated in nanoindentation tests, whereas an opposite tendency is found for pristine graphene.

To examine the observed discrepancy between uniaxial tensile and nanoindentation studies, we compare the evolution of atomic configuration in the nanoindentation simulation with that in the tensile simulation. We find that the graphene sheets under indentation often sustain loads after crack nucleation. Fig. 4(a) shows the evolution of atomic configurations for a symmetric tilt GB with an angle of 5.7°. The initial crack nucleation occurs at 3.54 nm, but the graphene sheet sustains the load up to the deflection of 4.6 nm, until a catastrophic failure occurs beyond 5.0 nm. The pre-stress around the 5–7 defects enables crack nucleation at a small deflection, but fast-diminishing stress away from the center of the indenter does not provide a sufficient driving force for catastrophic crack propagation. A crack grows in a stable manner until it reaches the size of the indenter radius. The overestimation of strength of GB is attributed to the delay in catastrophic crack growth after nucleation. The amount of delay depends on the atomic configuration near the crack tip, and this leads to the observed variation in strength as a function of distance D. On the contrary, the onset of crack nucleation is immediately captured by the failure in the uniaxial tension simulation, as depicted in Fig. 4(b). The homogeneous stress field provides a driving force for unstable crack growth, followed by fracturing right after crack nucleation. The observed crack growth can be explained by the relationship between the crack size and the energy release rate from linear elastic fracture mechanics theory. We have derived a formula for the energy release rate as a function of contact radius (r_1) and crack length (a) (see section S7 and Fig. S10 of the ESI†). When the distance (r) from the center of the indenter tip is larger than r_1, the stress field decays as $1/r$ because of the force balance in the vertical direction (indentation force $F = 2\pi r t \sigma(r) \sin \theta$ where t is the thickness of graphene and $\sin \theta \approx r_1/R$). When the crack length (a) becomes larger than the contact radius (r_1), the potential energy is given as $\Delta U \approx \Delta U_1 + 2\pi t/E \int_{r_1}^{a} \sigma(r)^2 r\, dr = \Delta U_1 + F^2/2\pi t E \sin^2 \theta \ln a/r_1,$ where ΔU_1 is the potential energy change within the contact area. Accordingly, the energy release rate becomes

inversely proportional to the crack length, i.e. G(a) ∝ 1/a. Thus, crack growth becomes stable when the crack size is larger than the contact radius.

This delayed crack propagation is not observed in pristine graphene because very high stress is required for crack nucleation in the absence of pre-stress. Upon crack nucleation, large accumulated elastic energy is released to instantaneously create a crack bigger than the indenter radius. Similarly, in the high-tilt angle GB sample, the pre-stress of the 5–7 defects is effectively cancelled. Thus, the high-tilt angle GB fails in a manner similar to that of pristine graphene, and its strength estimation is close to the value of pristine graphene as shown in Fig. 3(a) and (b). To summarize, nanoindentation has a tendency to underestimate the strength of pristine graphene due to the biaxial stress state, while it overestimates the strength of GB because of the delayed crack propagation. This gives an explanation on why the strength difference between pristine and polycrystalline graphene is underestimated in some literature.[32]

We also investigate the effect of misalignment of the indenter tip on the strength of GB. We measure the failure force as a function of the distance (S) away from the GB line (see the inset of Fig. 5(a)). All stress–strain curves are depicted in Fig. S8 and S9 in the ESI.† In the case of high-tilt angle GBs, the failure force approaches that of pristine graphene at a distance much smaller than the indenter radius (50 Å), while it does so at a larger distance for low-tilt angle GBs. This distance dependence can be understood in terms of pre-stress generated from the 5–7 defect array. The dipolar pre-stress of a single 5–7 defect is not effectively counterbalanced for lowangle GBs, for which the inter-defect distance is relatively large. In contrast, in high-angle GBs in which 5–7 defects are located close to each other, the dipolar pre-stress field is effectively cancelled. Moreover, we find that the failure occurs away from the GB in the bi-crystal graphene when the distance S is similar to the indenter radius, regardless of the indenter radius (see section S5 of the ESI). Fig. 6 shows the failure mechanism of the graphene sheet when the indenter is located away from the GBs for both symmetric and asymmetric GBs. The failure occurs near the center of the indenter tip even though the crack initiated near the 5–7 defect. This explains the high strength estimation in the case of indenter misalignment, as shown in Fig. 5.

Lee et al.[32] reported that the strength of GBs is comparable to the strength of pristine graphene regardless of the tilt angle, while Rasool et al.[30] reported that strength depends on the tilt angle. This difference might be caused by the different indenter radii used in those studies. The indenter radius in the former study is 26–38 nm; a small misalignment of ~10 nm could have led to an overestimation of the strength. In contrast, Rasool et al. used an indenter with a radius of 115 nm, which was used for correct strength estimation even for larger misalignment. In addition, Lee et al. attributed this phenomenon to the discrepancy of atomic structures between the symmetric and asymmetric GB. However, we observed that symmetric and asymmetric GBs show the same tendency of strength estimations (see Fig. 3(c) and (d)).

Conclusions

In conclusion, we find that the strengths of polycrystalline graphene are locally measureable quantities that are only valid within the radius of the indenter, because nanoindentation produces a sharp stress concentration near the indenter tip. In contrast to tensile simulation, bi-crystalline graphene can sustain the indenter load beyond the crack initiation. Thus, the strength estimated from nanoindentation is not suitable for mapping into the tensile strength. The strength estimation of polycrystalline graphene can vary as the indenter location changes along the GB line, which explains the scatter obtained in previous experimental studies. Also, we find that nanoindentation has a tendency to underestimate the pristine graphene strength and overestimate the polycrystalline graphene strength. This gives another explanation for how nanoindentation experiments can underestimate the difference in strength between polycrystalline graphene[37] and pristine graphene.

Our findings elucidate the problem of mapping the strength estimated from the nanoindentation fracture force to the strength of the material under tensile loading. Moreover, the difference between fracture mechanisms in the two different loading modes can serve as a guide to design mechanically reliable devices based on 2D materials.

Acknowledgements

References

1 J. S. Bunch, A. M. van der Zande, S. S. Verbridge, I. W. Frank, D. M. Tanenbaum, J. M. Parpia, H. G. Craighead and P. L. McEuen, Science, 2007, 315, 490–493.

2 C. Lee, X. D. Wei, J. W. Kysar and J. Hone, Science, 2008, 321, 385–388.

3 S. P. Koenig, N. G. Boddeti, M. L. Dunn and J. S. Bunch, Nat. Nanotechnol., 2011, 6, 543–546.

4 G. Lopez-Polin, C. Gomez-Navarro, V. Parente, F. Guinea, M. I. Katsnelson, F. Perez-Murano and J. Gomez-Herrero, Nat. Phys., 2015, 11, 26–31.

5 S. Berciaud, S. Ryu, L. E. Brus and T. F. Heinz, Nano Lett., 2009, 9, 346–352.

6 D. Garcia-Sanchez, A. M. van der Zande, A. S. Paulo, B. Lassagne, P. L. McEuen and A. Bachtold, Nano Lett., 2008, 8, 1399–1403.

7 J. S. Bunch, S. S. Verbridge, J. S. Alden, A. M. van der Zande, J. M. Parpia, H. G. Craighead and P. L. McEuen, Nano Lett., 2008, 8, 2458–2462.

8 Q. K. Yu, J. Lian, S. Siriponglert, H. Li, Y. P. Chen and S. S. Pei, Appl. Phys. Lett., 2008, 93.

9 A. Reina, X. T. Jia, J. Ho, D. Nezich, H. B. Son, V. Bulovic, M. S. Dresselhaus and J. Kong, Nano Lett., 2009, 9, 30–35.

10 Y. Lee, S. Bae, H. Jang, S. Jang, S. E. Zhu, S. H. Sim, Y. I. Song, B. H. Hong and J. H. Ahn, Nano Lett., 2010, 10, 490–493.

11 S. Bae, H. Kim, Y. Lee, X. Xu, J.-S. Park, Y. Zheng, J. Balakrishnan, T. Lei, H. Ri Kim, Y. I. Song, Y.-J. Kim, K. S. Kim, B. Ozyilmaz, J.-H. Ahn, B. H. Hong and S. Iijima, Nat. Nanotechnol., 2010, 5, 574–578.

12 X. Li, W. Cai, J. An, S. Kim, J. Nah, D. Yang, R. Piner, A. Velamakanni, I. Jung, E. Tutuc, S. K. Banerjee, L. Colombo and R. S. Ruoff, Science, 2009, 324, 1312–1314.

13 S. Malola, H. Häkkinen and P. Koskinen, Phys. Rev. B: Condens. Matter, 2010, 81, 165447.

14 O. V. Yazyev and S. G. Louie, Phys. Rev. B: Condens. Matter, 2010, 81, 195420.

15 J. Cervenka, M. I. Katsnelson and C. F. J. Flipse, Nat. Phys., 2009, 5, 840–844.

16 J. Avila, I. Razado, S. Lorcy, R. Fleurier, E. Pichonat, D. Vignaud, X. Wallart and M. C. Asensio, Sci. Rep., 2013, 3, 2439.

17 J. C. Meyer, A. K. Geim, M. I. Katsnelson, K. S. Novoselov, T. J. Booth and S. Roth, Nature, 2007, 446, 60–63.

18 P. Y. Huang, C. S. Ruiz-Vargas, A. M. van der Zande, W. S. Whitney, M. P. Levendorf, J. W. Kevek, S. Garg, J. S. Alden, C. J. Hustedt, Y. Zhu, J. Park, P. L. McEuen and D. A. Muller, Nature, 2011, 469, 389–392.

19 K. Kim, Z. Lee, W. Regan, C. Kisielowski, M. F. Crommie and A. Zettl, ACS Nano, 2011, 5, 2142–2146.

20 K. Kim, V. I. Artyukhov, W. Regan, Y. Y. Liu, M. F. Crommie, B. I. Yakobson and A. Zettl, Nano Lett., 2012, 12, 293– 297.

21 J. R. Xiao, J. Staniszewski and J. W. Gillespie Jr., Compos. Struct., 2009, 88, 602–609.

22 J. F. Zhang, J. J. Zhao and J. P. Lu, ACS Nano, 2012, 6, 2704– 2711.

23 J. Han, S. Ryu, D. Sohn and S. Im, Carbon, 2014, 68, 250– 257.

24 T. H. Liu, C. W. Pao and C. C. Chang, Carbon, 2012, 50, 3465–3472.

25 L. J. Yi, Z. N. Yin, Y. Y. Zhang and T. C. Chang, Carbon, 2013, 51, 373–380.

26 Y. J. Wei, J. T. Wu, H. Q. Yin, X. H. Shi, R. G. Yang and M. Dresselhaus, Nat. Mater., 2012, 11, 759–763.

27 R. Grantab, V. B. Shenoy and R. S. Ruoff, Science, 2010, 330, 946–948.

28 Y. I. Jhon, S. E. Zhu, J. H. Ahn and M. S. Jhon, Carbon, 2012, 50, 3708–3716.

29 C. S. Ruiz-Vargas, H. L. L. Zhuang, P. Y. Huang, A. M. van der Zande, S. Garg, P. L. McEuen, D. A. Muller, R. G. Hennig and J. Park, Nano Lett., 2011, 11, 2259– 2263.

30 H. I. Rasool, C. Ophus, W. S. Klug, A. Zettl and J. K. Gimzewski, Nat. Commun., 2013, 4, 2811.

31 A. Zandiatashbar, G. H. Lee, S. J. An, S. Lee, N. Mathew, M. Terrones, T. Hayashi, C. R. Picu, J. Hone and N. Koratkar, Nat. Commun., 2014, 5, 3186.

32 G. H. Lee, R. C. Cooper, S. J. An, S. Lee, A. van der Zande, N. Petrone, A. G. Hammerherg, C. Lee, B. Crawford, W. Oliver, J. W. Kysar and J. Hone, Science, 2013, 340, 1073– 1076.

33 Z. Song, V. I. Artyukhov, J. Wu, B. I. Yakobson and Z. Xu, ACS Nano, 2015, 9, 401–408.

34 Z. D. Sha, Q. Wan, Q. X. Pei, S. S. Quek, Z. S. Liu, Y. W. Zhang and V. B. Shenoy, Sci. Rep., 2014, 4, 7437.

35 S. J. Stuart, A. B. Tutein and J. A. Harrison, J. Chem. Phys., 2000, 112, 6472–6486.

36 S. Plimpton, J. Comput. Phys., 1995, 117, 1–19.

37 X. Jia, J. Campos-Delgado, M. Terrones, V. Meunier and M. S. Dresselhaus, Nanoscale, 2011, 3, 86–95.

38 Z. D. Sha, S. S. Quek, Q. X. Pei, Z. S. Liu, T. J. Wang, V. B. Shenoy and Y. W. Zhang, Sci. Rep., 2014, 4, 5991.

39 L. He, S. Guo, J. Lei, Z. Sha and Z. Liu, Carbon, 2014, 75, 124–132.

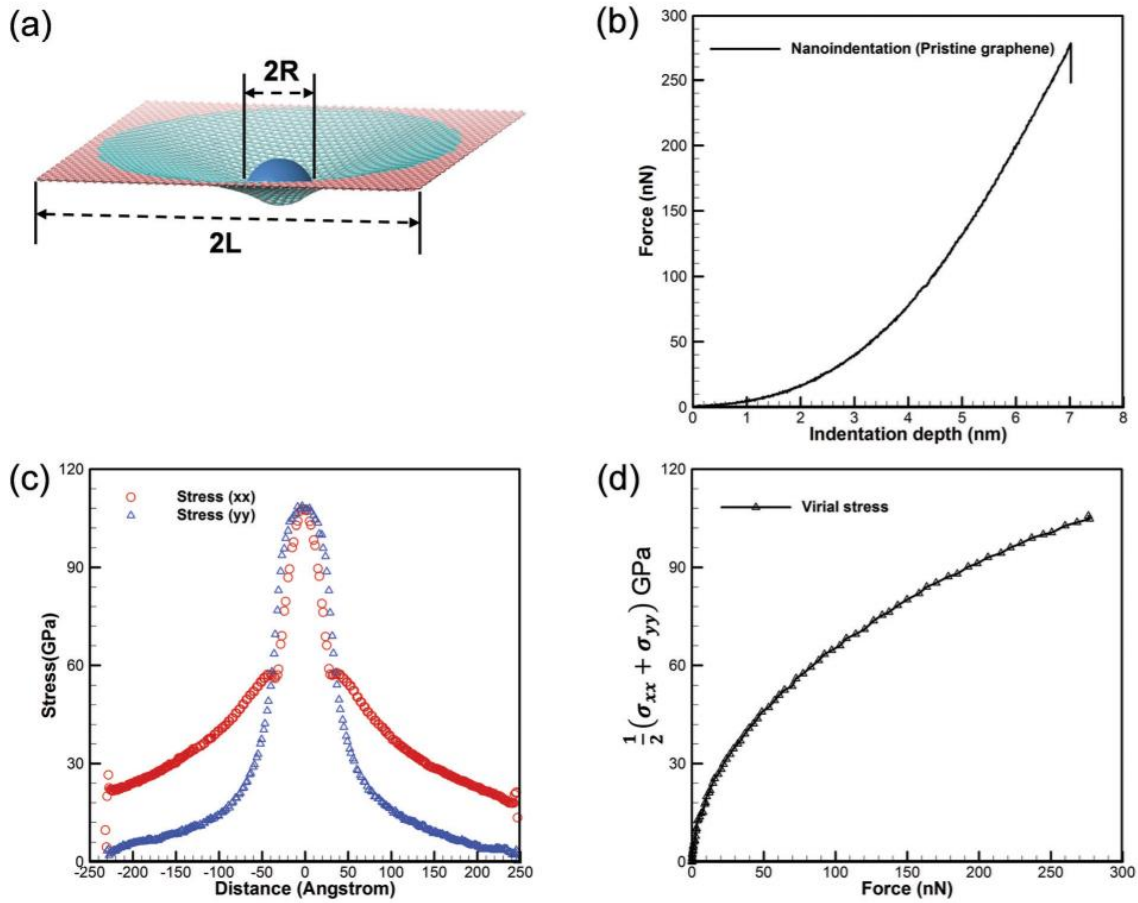40 B. I. Costescu and F. Grater, Phys. Chem. Chem. Phys., 2014, 16, 12582–12590.

Fig. 1 (a) Schematic of nanoindentation simulations. (b) Force–displacement curve obtained from the nanoindentation of pristine graphene. (c) In-plane stress distribution along the central line of the graphene sheet. (d) Stress *versus* force curve obtained from (b) and (c) at various deflections.
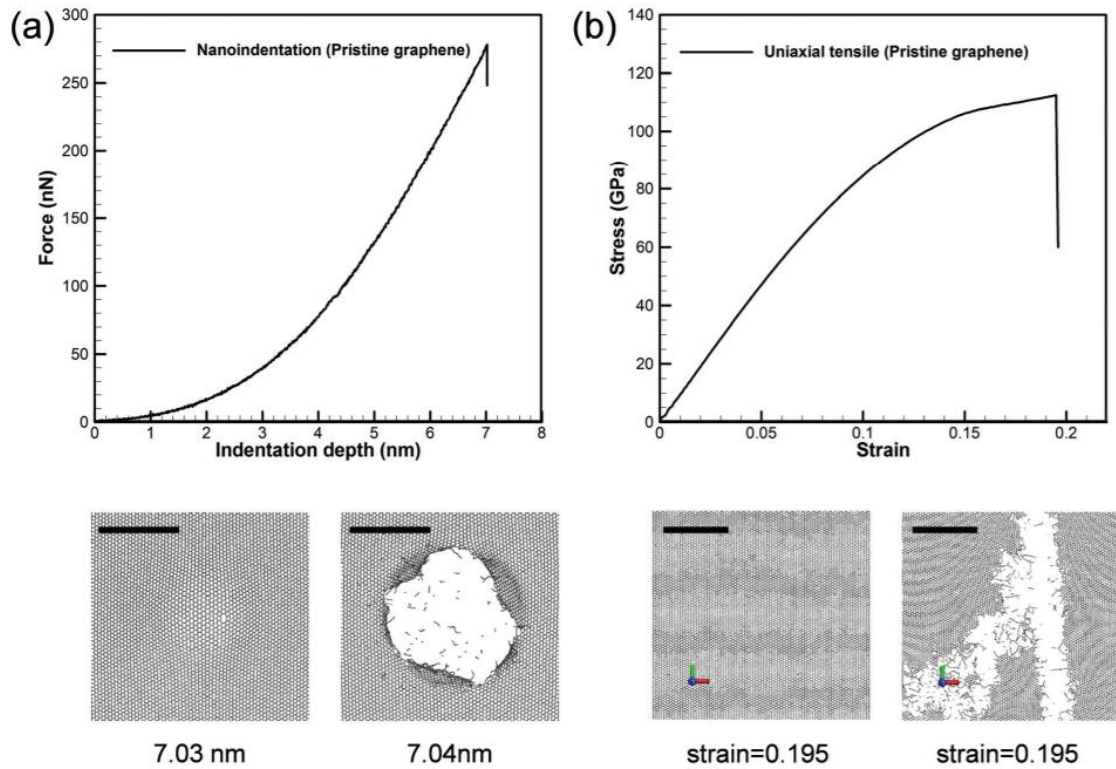

7.03 nm   7.04nm   strain=0.195   strain=0.195

Fig. 2 (a) Force–deflection curve of pristine graphene from nanoindentation and atomic configurations at the indentation depth at fracture. (b) Stress–strain curve of pristine graphene from uniaxial tensile simulation and atomic configurations at fracture. Scale bars represent 50 Å.
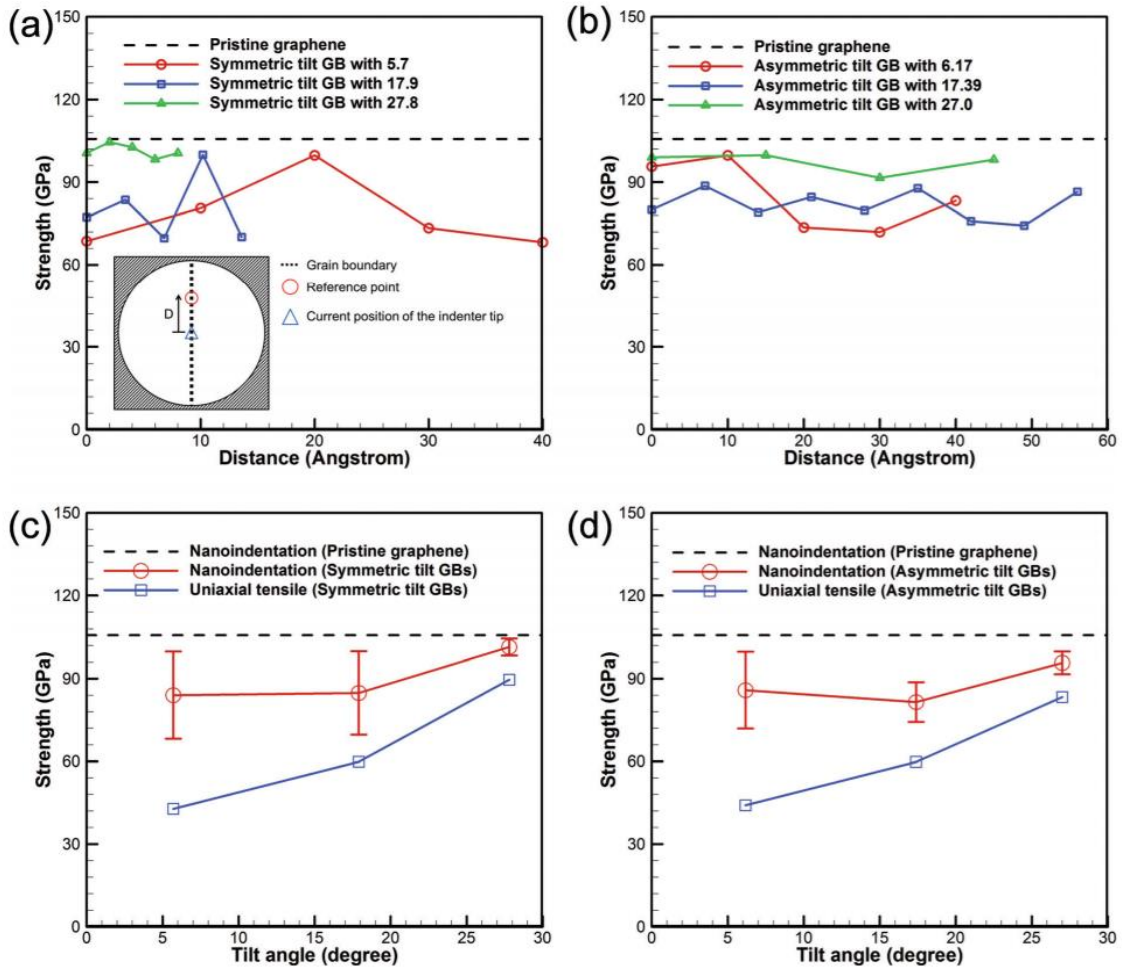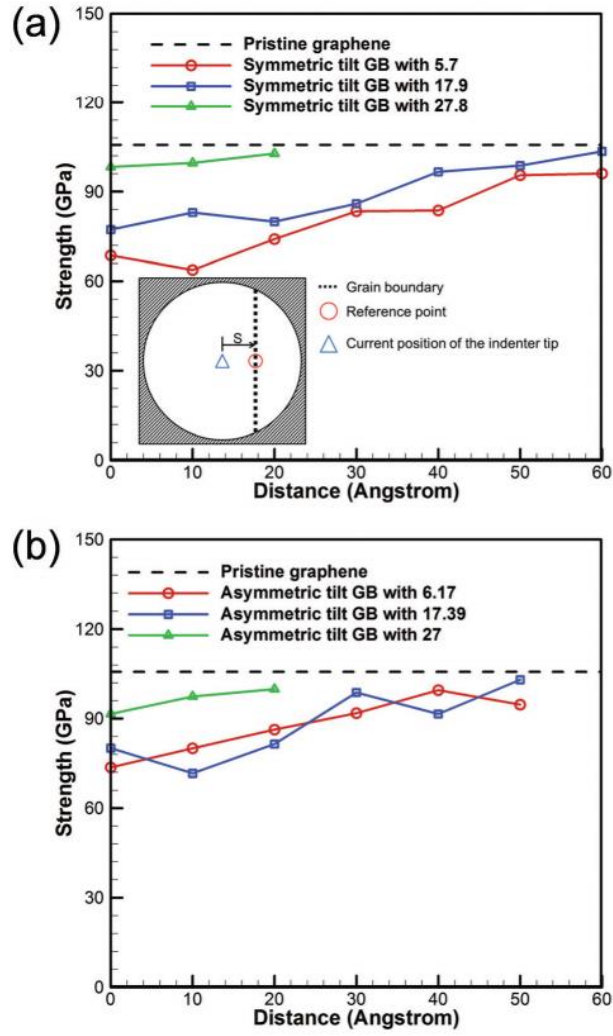
**Fig. 3** Strength estimation as a function of the indenter position (D) for (a) symmetric tilt GBs and (b) asymmetric tilt GBs. The inset of (a) is a schematic diagram of a nanoindentation simulation in which the indenter tip is located on the GB line. The strength estimation from nanoindentation and uniaxial tensile simulations is plotted together for (c) symmetric tilt GBs and (d) asymmetric tilt GBs.
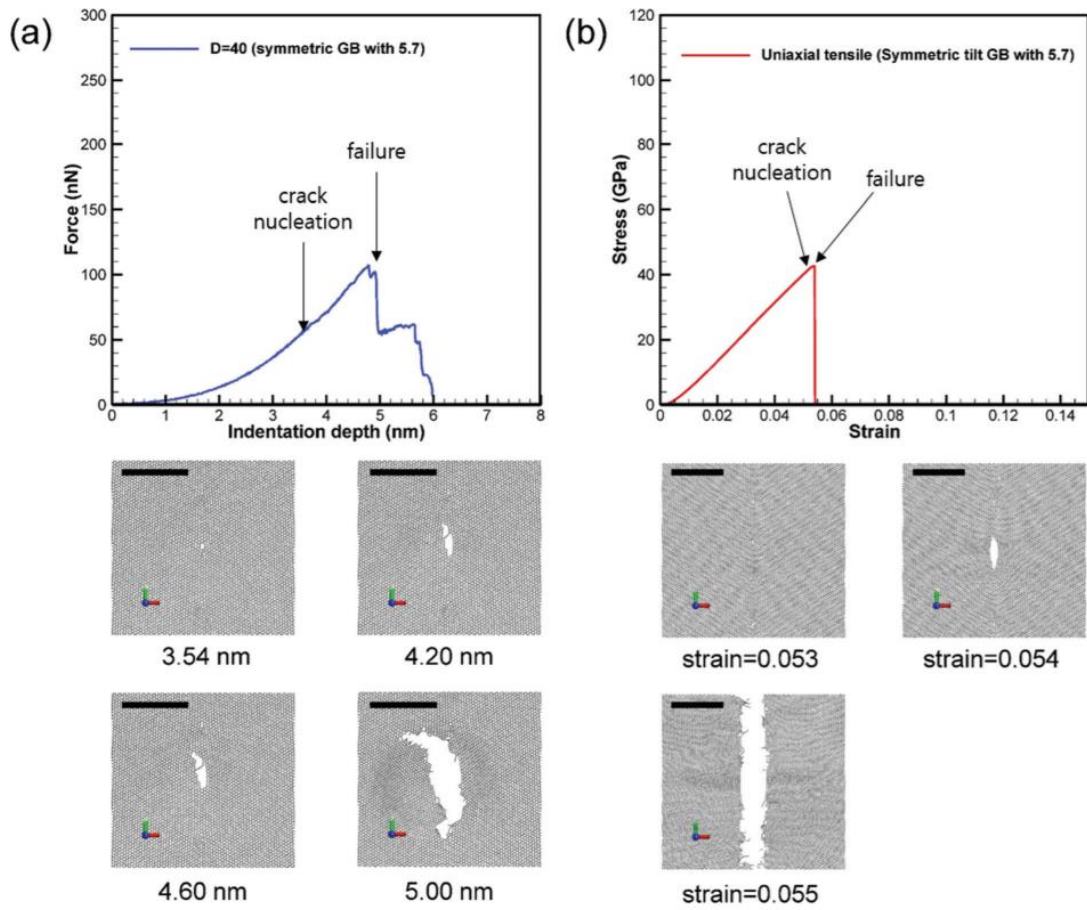
Fig. 4 Atomic configurations at various indentation depths or tensile strains. (a) Force−deflection curve from nanoindentation and atomic configurations at various deflections. Failure occurs at significantly further indentation after the crack nucleation. (b) Stress−strain curve from uniaxial tension and atomic configurations at various indentation depths. Failure occurs immediately after the crack nucleation. Scale bars represent 50 Å.

Fig. 5 Strength estimation as a function of the indenter position (S) for (a) symmetric tilt GBs and (b) asymmetric tilt GBs.
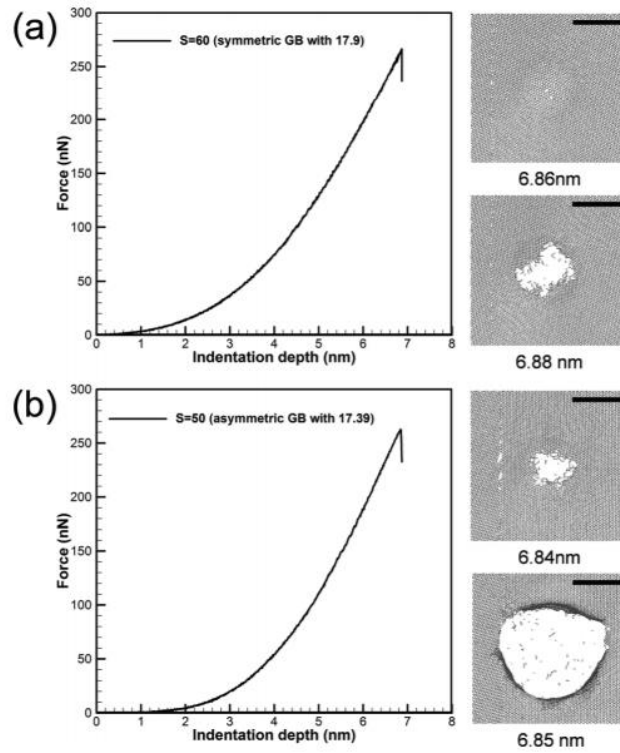
Fig. 6 Atomic configurations at fracture for crack propagation generated away from the GB. (a) Force–deflection curve and atomic configurations of (a) symmetric tilt GBs with an angle of 17.9° at the distance (*S*) of 6 nm, and (b) asymmetric tilt GBs with an angle of 17.39° at the distance (*S*) of 5 nm. Scale bars represent 50 Å.

Supplementary Information

Nanoindentation cannot accurately predict the tensile strength of graphene or other 2D materials

Jihoon Han [a,b], Nicola Pugno [c,d,e], and Seunghwa Ryu [a,*]

[a] Department of Mechanical Engineering, Korea Advanced Institute of Science and Technology (KAIST), 291 Daehak-ro, Yuseong-gu, Daejeon, 305-701, Republic of Korea
[b] Research Reactor Utilization Department, Korea Atomic Energy Research Institute, 898-111 Daedeok-daero, Yuseong-gu, Daejeon, 305-535, Republic of Korea
[c] Laboratory of Bio-Inspired and Graphene Nanomechanics, Department of Civil, Environmental and Mechanical Engineering, University of Trento, Via Mesiano 77, I-38123 Trento, Italy
[d] Centre for Materials and Microsystems, Fondazione Bruno Kessler, Via Sommarive 18, I-38123 Povo (Trento), Italy
[e] School of Engineering and Materials Science, Queen Mary University of London, Mile End Road, E1 4NS, London, UK

Contents

S1. Structures of symmetric and asymmetric tilt grain boundaries (GB)

* Corresponding author.   Tel.: +82-42-350-3019, Fax: +82-42-350-3059.

E-mail addresses: ryush@kaist.ac.kr (S. Ryu)

The polycrystalline graphene with symmetric tilt and asymmetric tilt GB is constructed by referring to the procedures depicted in Ref. 1 and Ref. 2, respectively. We construct a series of polycrystalline graphene with a misorientation angle between 0° and 30°. The structures of symmetric and asymmetric tilt GBs at three grain misorientation angle are presented in Figs. S1(a)−(c) and Figs. S1(d)−(f), respectively. GBs, which are composed of series of 5-7 defects, are located on the center of the polycrystalline graphene.

S2. Verification of loading speed

To verify the effect of loading speed on the mechanical response of graphene sheet, a series of nanoindentation simulations are conducted under loading speed ranged from 0.02 to 0.1 Å/ps. Fig. S2 shows the force-displacement curves with respect to the loading speed of indenter for the indenter tip located on the center of pristine graphene. The maximum load and indentation load slightly increases with loading speed but the changes are not remarkable. In the remaining part of this study, the loading speed is chosen to be 0.02 Å/ps.

S3. Uniaxial and biaxial tensile simulations of pristine graphene

We performed biaxial tensile simulation in order to directly compare with the strength of the nanoindentation simulation. Before the tensile loading test, samples are initially equilibrated for 10 ps using NPT (isothermal-isobaric) ensemble at 300K. For uniaxial tensile simulations, uniaxial tension along the x-axis (perpendicular to the GBs) is applied using NPT which allows the zero pressure in the y direction to mimic the traction free boundary condition. For biaxial tensile simulations, the graphene film is stretched in both x- and y-directions until it fails completely under NVT (canonical) ensemble. Simulations boxes are stretched by pulling on both sides (LAMMPS; ref. 4 command: fix/deform). Periodic boundary condition is applied in all direction. All samples are stretched at a constant strain rate of 10^9 s^{-1}. The stress is averaged over 1 ps at each strain increment to eliminate thermal fluctuations.

Fig. S3 depicts the stress-strain curves of uniaxial and biaxial tensile simulations. The estimated strength of biaxial tensile is 105 GPa which shows good agreement with that of the

nanoindentation simulation (see Fig. 1(d)). In comparison with uniaxial tensile, Fig. S3 shows that the biaxial strength is lower than the uniaxial strength. Therefore, the strength estimated by nanoindentation can be underestimated because the graphene is subjected to equibiaxial tensile load generated by an indenter.

S4. Comparison of stress distribution between pristine and polycrystalline graphene

For comparison, indentation simulations are carried out to investigate the stress distribution of pristine and polycrystalline graphene under the same simulation conditions. The non-uniform stress distribution of pristine and symmetric tilt GB with the angle of 5.7° are plotted together which is obtained slightly before the rupture as shown in Fig. S4(a). The stress is defined by the average between σ_{xx} and σ_{yy}. We observed that the stress decreases with distance from the center of indenter tip. For the symmetric tilt GB, there is a very sharp peak in the stress distribution due to the pre-stress around 5-7 defects. A sequence of snapshots shows that rupture starts at lower indentation depth (see Fig. S4(d)).

S5. Size effect of indenter radius on mechanical response under nanoindentation

A series of nanoindentation simulations with the indenter radius of 2 nm is performed to investigate the size effect of indenter radius. We obtain the force-stress curve for the pristine graphene under nanoindentation with the same indenter radius, as shown in Fig. S5(a). The failure force is converted into the strength using the stress-force relationship. All stress-strain curves are shown in Fig. S5(b). We estimate the strength as a function of distance away from the GB line (see the inset of Fig. 5(a)). As shown in Fig. S5(c)), the failure strength approaches that of pristine graphene as the distance which becomes in close proximity to the indenter radius (~2 nm). The smaller indenter radius leads to more sharp stress concentration within the indenter radius. Hence, the strength can be overestimated at a smaller misalignment. It note that there is the prospect of high strength estimation in the case of indenter misalignment. Therefore, the estimated strength is close to that of pristine graphene at a distance of indenter radius, regardless of indenter size.

S6. Force-displacement curves of polycrystalline graphene

The force-displacement curves of polycrystalline graphene with symmetric and asymmetric tilt GBs are presented in Figs. S6 and S9. First, we examine the sensitivity of strength according to the position of the indenter by moving the location of indenter along the GB (see the inset of Fig. 3(a)). The force-displacement curves of symmetric and asymmetric tilt GBs are presented in Figs. S6 and S7, respectively. The force-displacement curve is significantly dependent on the location of the indenter. Compared to the mean value of the strength, the strength is varied by up to about 16%, the position of the indenter at low-tilt angle GBs (see Figs. 3(c) and (d)). Note that this difference is not caused by a statistical error of molecular dynamics since the difference is larger than the statistical error at each misorientation angle.

Second, in order to investigate the effect of a misaligned indenter on the strength of polycrystalline graphene, GB line is shifted from the position of indenter corresponds to the geometric center of graphene sheet (see the inset of Fig. 5(a)). The force-displacement curves of symmetric and asymmetric tilt GBs, according to the distance S, are presented in Figs. S8 and S9, respectively. We observe that the strength is proportional to the distance and approaches that of pristine graphene (see Fig. 5).

S7. Stability of crack

In the linear elastic fracture mechanics, the energy release rate for crack growth $G(a)$ is given as $\partial U / \partial a$, where ∂U is the infinitesimal change in potential energy due to the existing crack with length $2a$. Under uniaxial tension, it is known that $\Delta U = \dfrac{\pi a^2 \sigma_0^2 t}{E}$ where E, t and σ_0 refer to the Young's modulus, thickness, and the applied stress, respectively. Thus, the energy release rate is proportional to a, i.e. $G(a) \propto a$, and $\dfrac{\partial G}{\partial a} > 0$. This explains why the crack growth is unstable for uniaxial tension, as depicted in Fig. 4 (b).

On the contrary, the stress field near the indenter tip is highly concentrated around the tip. It is known that the stress field for $r < r_1$ is approximately constant where r_1 is the radius of contact area[3] (See Fig. S10). For $r > r_1$, stress field $\sigma(r)$ decays as $1/r$ because of the force balance in the vertical direction $\left(F = 2\pi r t \sigma(r)\sin\theta\right)$. Note that $\Delta U \approx \dfrac{\pi a^2 \sigma_0^2 t}{E}$ when $a < r_1$. On the other hand, $\Delta U \approx \Delta U_1 + \dfrac{2\pi t}{E}\int_{r_1}^{a}\sigma(r)^2\, r dr = \Delta U_1 + \dfrac{F^2}{2\pi t E \sin^2\theta}\ln\dfrac{a}{r_1}$ when $a > r_1$ where ΔU_1 is the potential energy change within the contact area. When a is larger than r_1, the energy release rate becomes inversely proportional to a, i.e. $G(a) \propto \dfrac{1}{a}$, and $\dfrac{\partial G}{\partial a} < 0$. Thus, crack growth becomes stable when the crack size is larger than r_1. This explains why the crack does not grow immediately after the nucleation for the low-angle GBs in Fig. 4 (a). At a small indentation depth, a crack can nucleate from the 5-7 defect where pre-stress is high, but it does not grow beyond the radius of contact r_1. r_1 increases as indentation depth increases further, which is followed by gradual crack growth. The ultimate fracture occurs once the crack size becomes comparable to the indenter radius.

For the pristine graphene or high-angle GBs, the crack nucleates at high indentation depth when stored elastic energy is very high and r_1 is comparable to indenter radius. Then, crack growth immediately up to the indenter radius, and fracture occurs simultaneously with crack nucleation, as shown in Fig. 2 (a).

References

1. Y. J. Wei, J. T. Wu, H. Q. Yin, X. H. Shi, R. G. Yang and M. Dresselhaus, Nat. Mater., 2012, 11, 759-763.

2. J. Han, S. Ryu, D. Sohn and S. Im, Carbon, 2014, 68, 250-257.

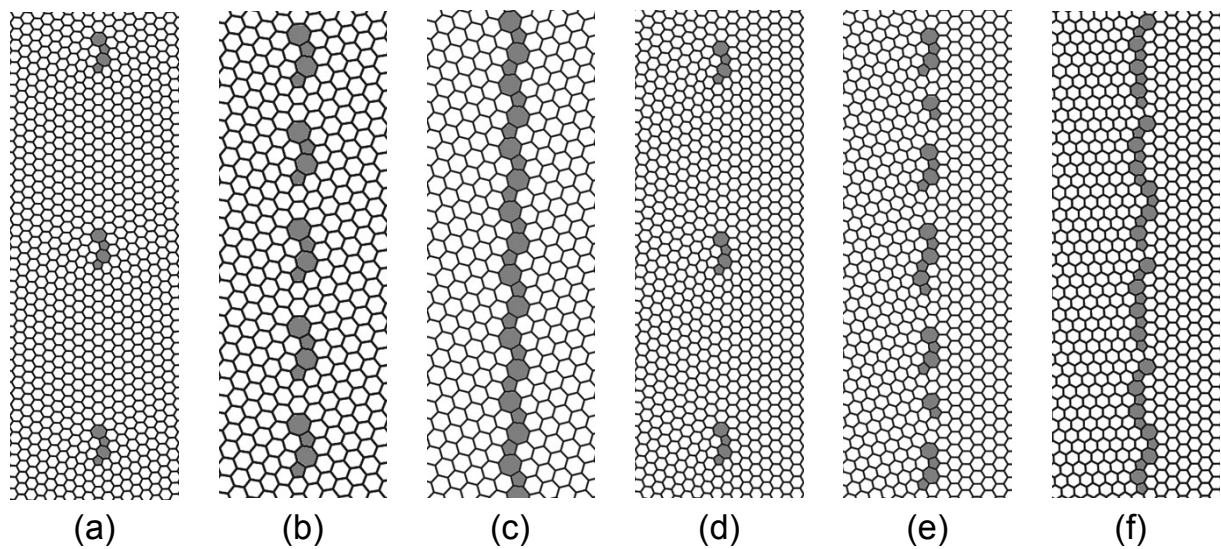3. M. R. Begley and T. J. Mackin, J. Mech. Phys. Solids., 2004, 52, 2005-2023.

Fig. S1 – The structures of armchair-oriented graphene grain boundaries at various misorientation angles in this study. (a)-(c) Typical structures of symmetric tilt GBs: (a) 5.7˚, (b) 17.9˚, and (c) 27.8˚. (d)-(f) Typical structures of asymmetric tilt GBs: (d) 6.17˚, (e) 17.39˚, and (f) 27.0˚.
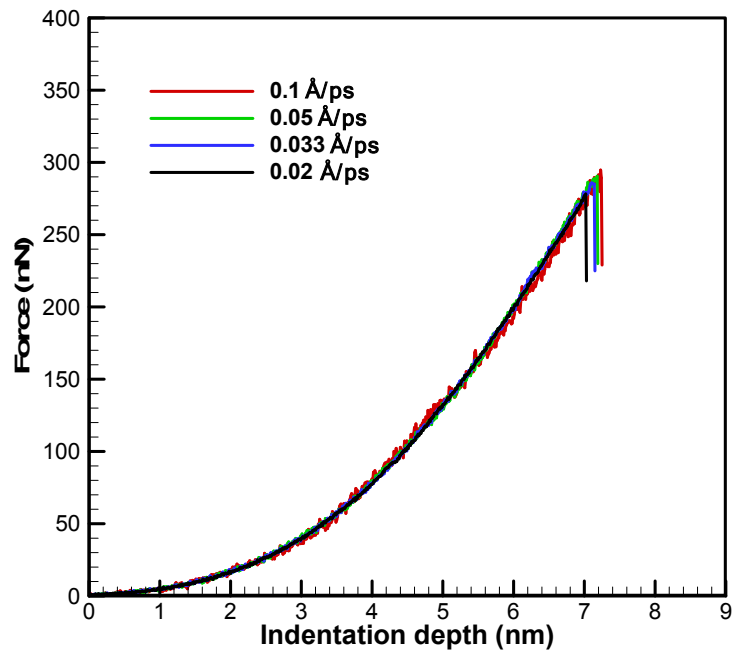
Fig. S2 – The force-displacement curves with respect to the loading speed of indenter for the indenter tip located on the center of pristine graphene.
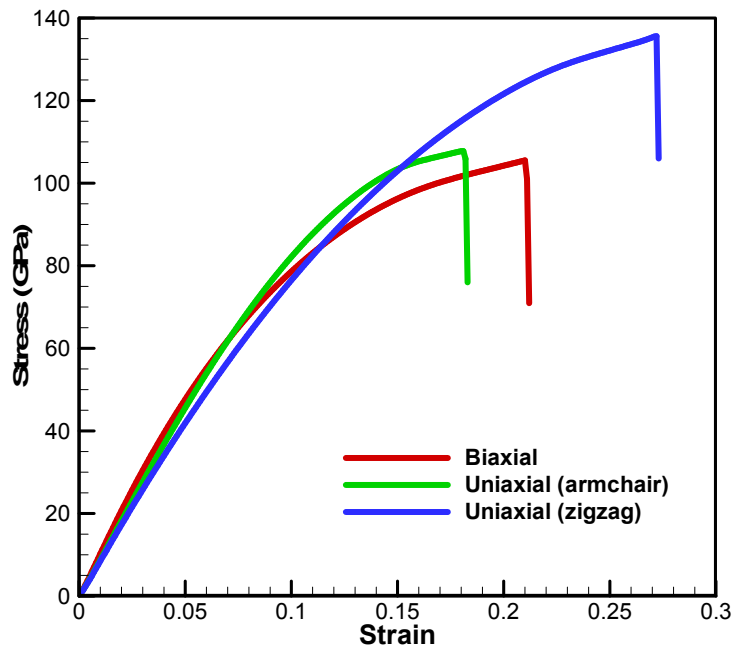
Fig. S3 – The stress-strain curves of uniaxial tensile and biaxial tensile simulations.
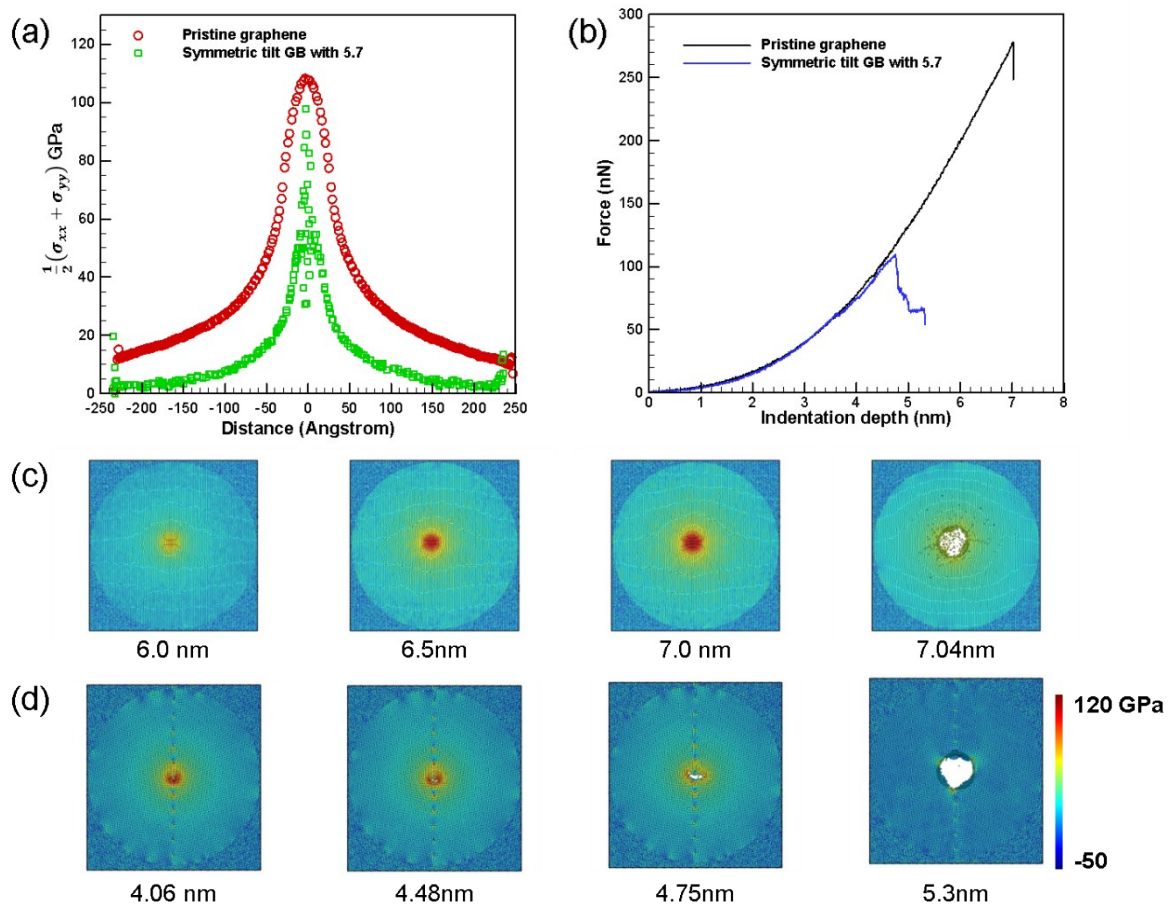
Fig. S4 – Comparison of stress distribution between pristine and bicrystal graphene. (a) In-plane stress distribution along the central line of graphene sheet on the verge of rupture. Stress represents the average between σ_{xx} and σ_{yy}. (b) Force-displacement curves of pristine and bi-crystal graphene are plotted together. The rupture process of (c) pristine graphene, and (d) symmetric tilt GB with 5.7°. The color contours indicate $\frac{1}{2}(\sigma_{xx} + \sigma_{yy})$.
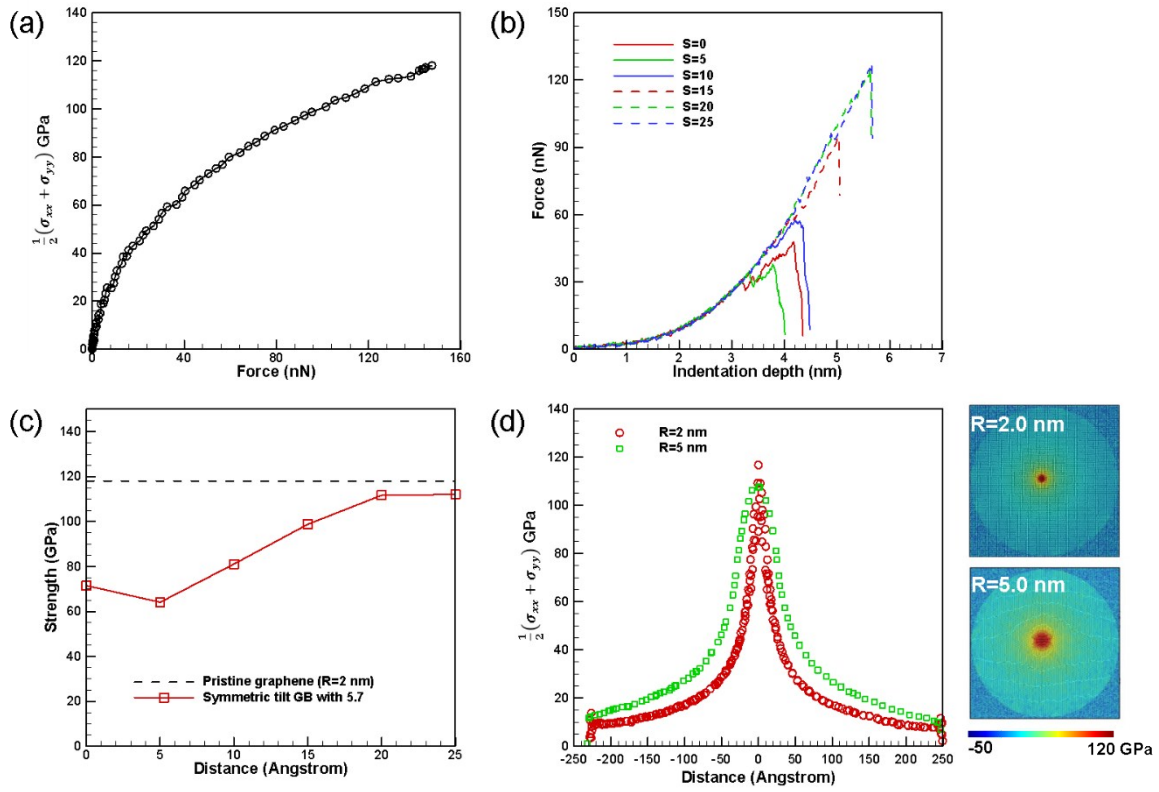
Fig. S5 – (a) Stress versus force curve for pristine graphene with the indenter radius of 5 nm. (b) The force-displacement curves of symmetric tilt GBs with various tilt angles. (c) Strength estimation as a function of indenter position (s) for symmetric tilt GB with 5.7°. (d) In-plane stress distribution along the central line of graphene sheet and atomic stress distributions on the verge of rupture. Stress represents the average between σ_{xx} and σ_{yy}. The color contours indicate the $\frac{1}{2}$ ($\sigma_{xx} + \sigma_{yy}$).
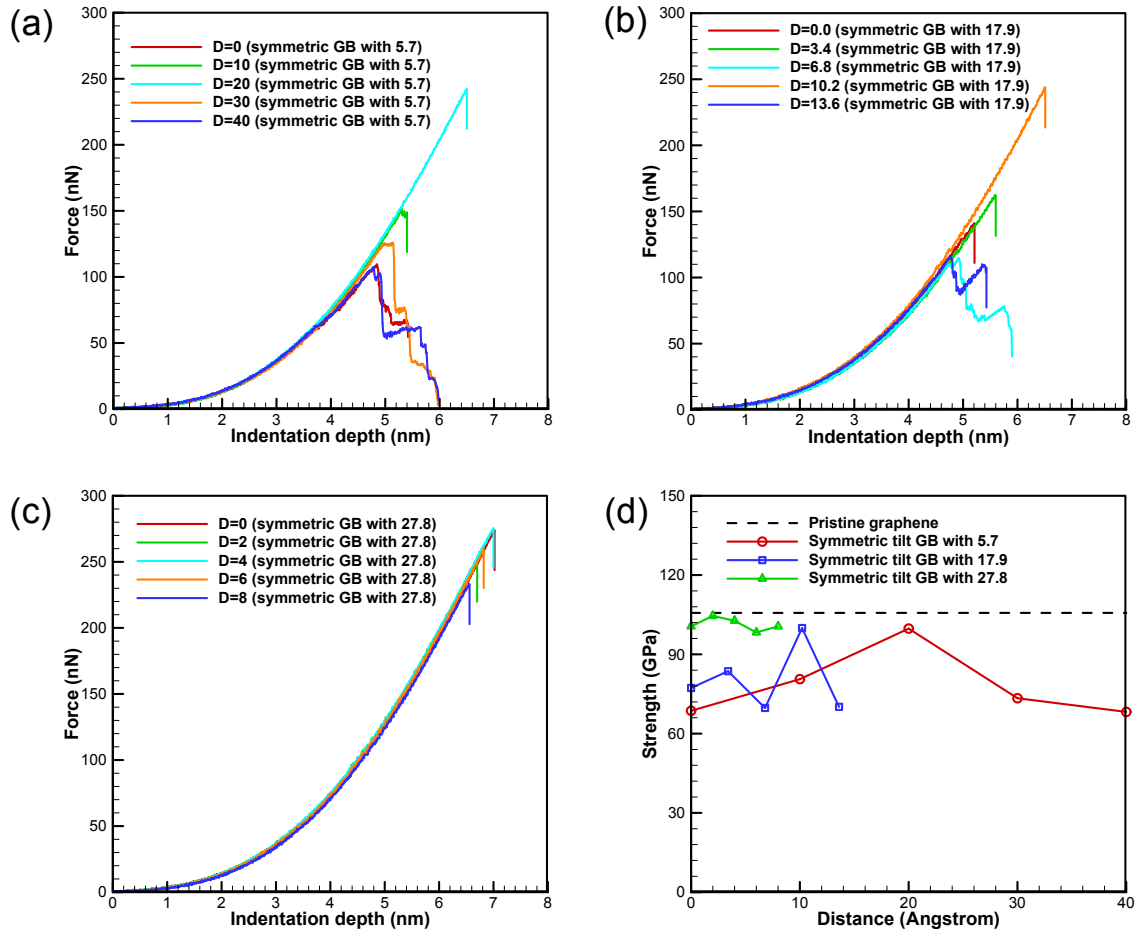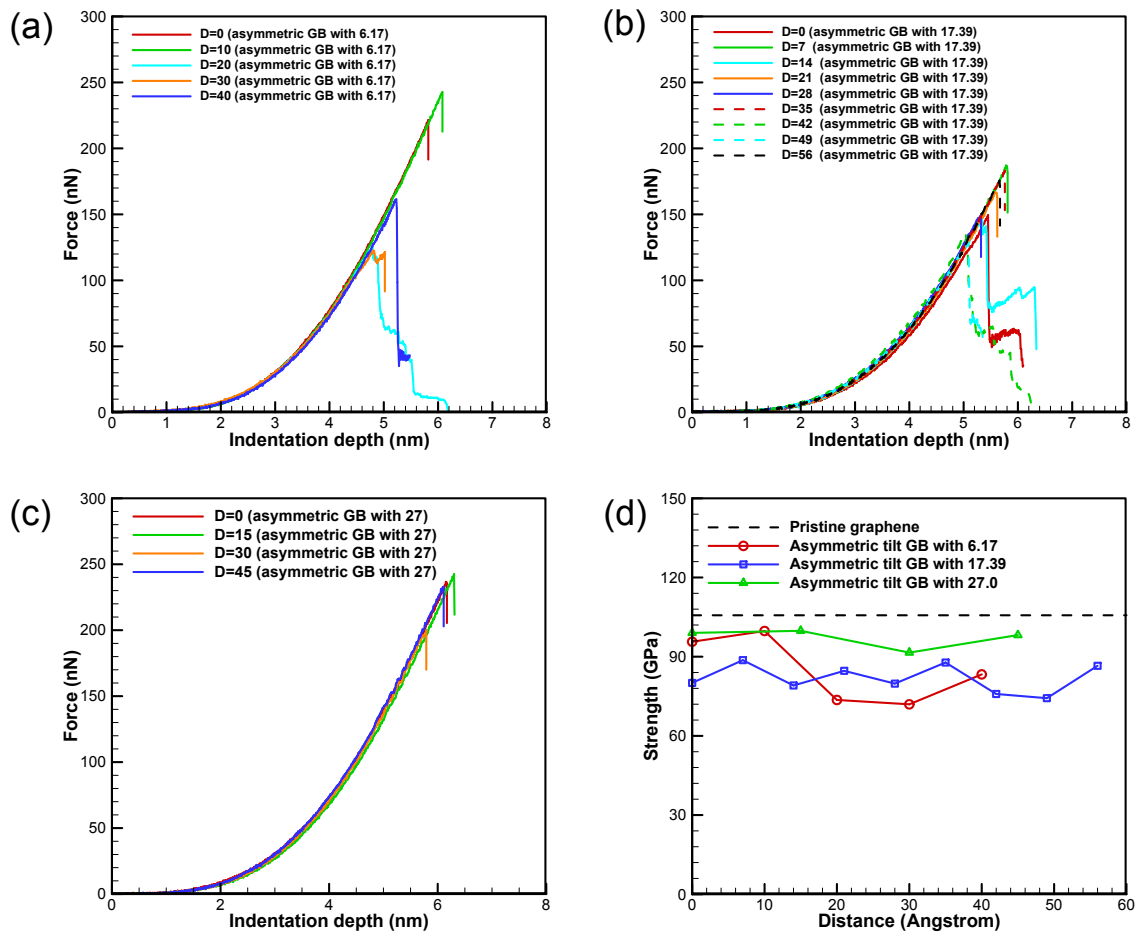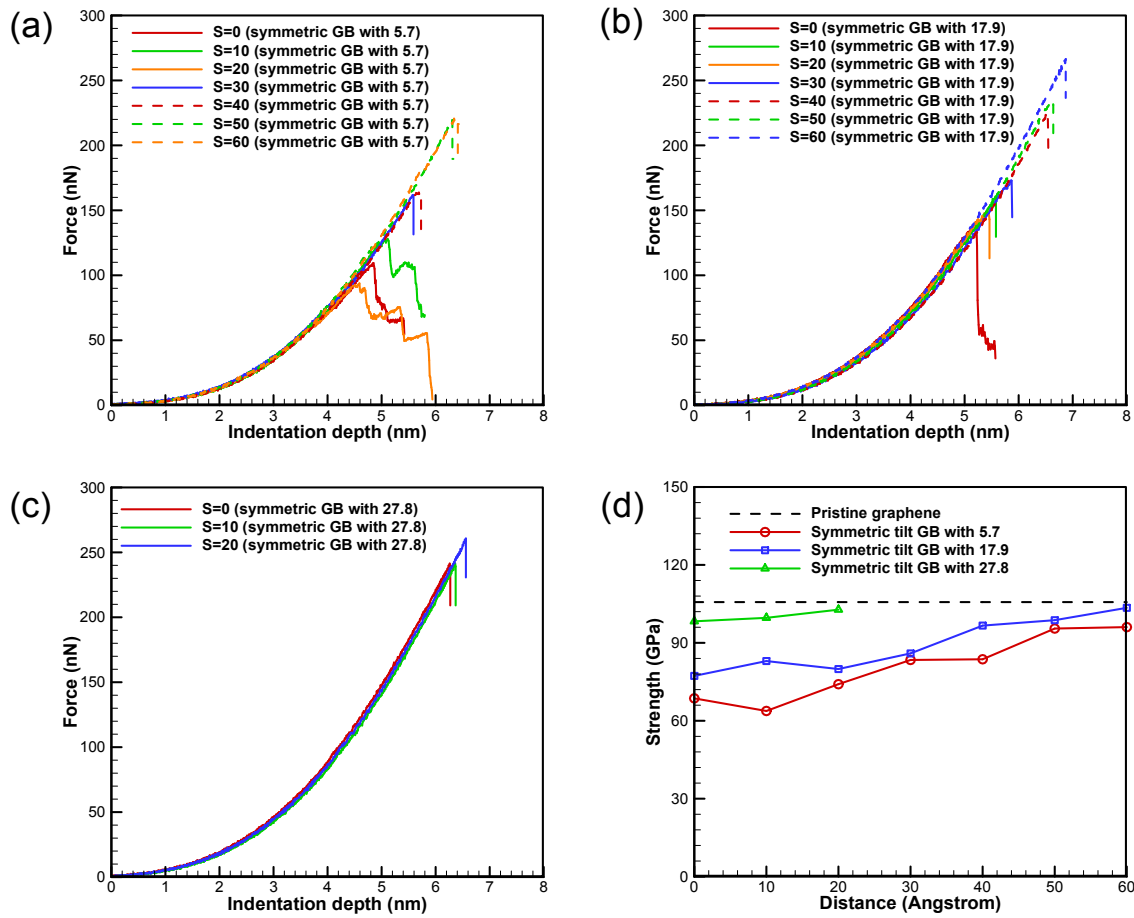
Fig. S6 – The force-displacement curves of symmetric tilt GBs with various tilt angles. The force-displacement curves of symmetric tilt GBs with respect to indenter location along the GB line: (a) 5.7˚, (b) 17.9 ˚, and (c) 27.8 ˚.

Fig. S7 – The force-displacement curves of asymmetric tilt GBs with various tilt angles. The force-displacement curves of asymmetric tilt GBs with respect to indenter location along the GB line: (a) 6.17˚, (b) 17.39 ˚, and (c) 27˚.
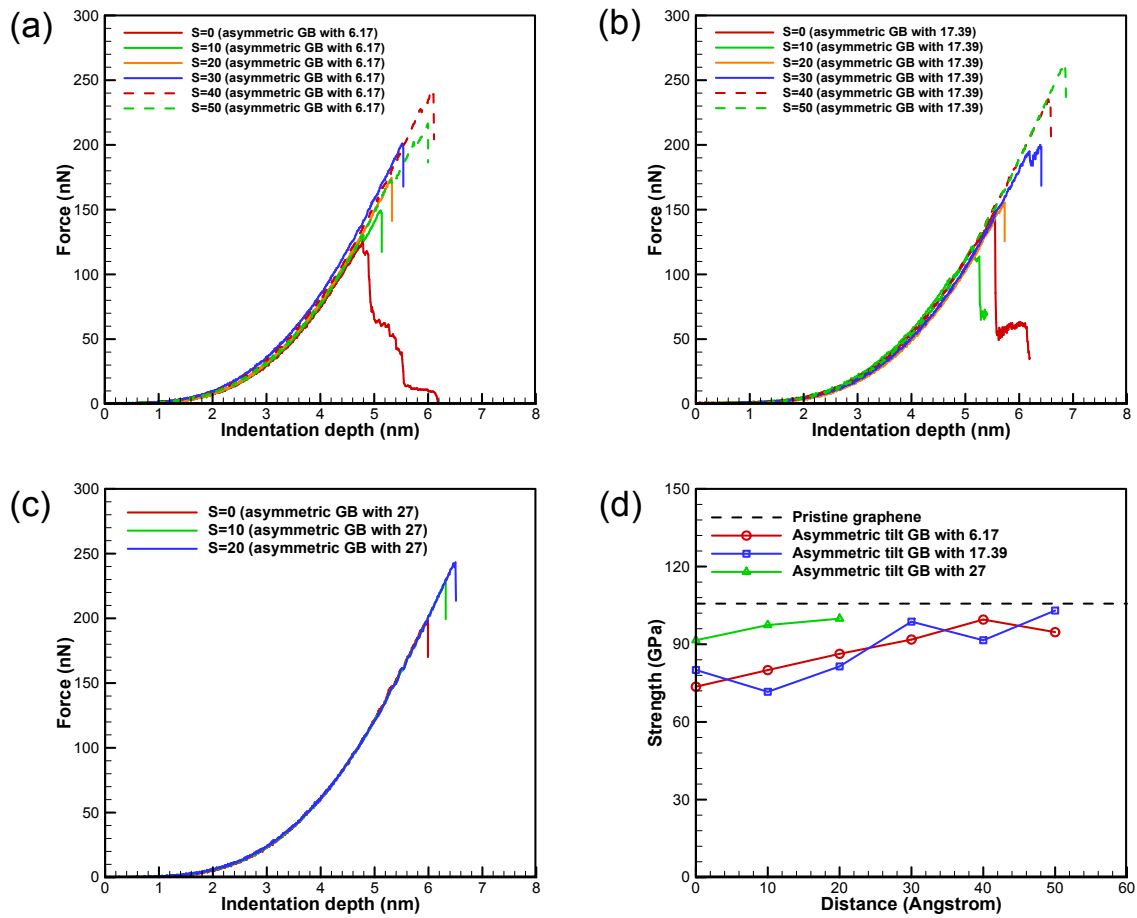
Fig. S8 – The force-displacement curves of symmetric tilt GBs with various tilt angles. The force-displacement curves of symmetric tilt GBs with respect to the distance S: (a) 5.7˚, (b) 17.9 ˚, and (c) 27.8˚.

Fig. S9 – The force-displacement curves of asymmetric tilt GBs with various tilt angles. The force-displacement curves of asymmetric tilt GBs with respect to the distance S: (a) 6.17°, (b) 17.39 °, and (c) 27°.
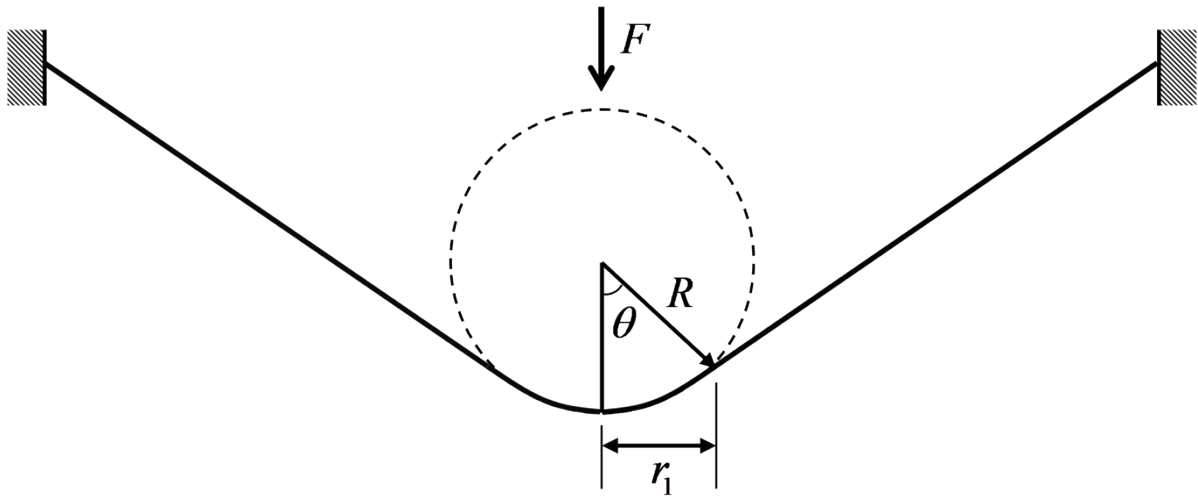
Fig. S10 – Schematic diagram of a spherical indenter with polycrystalline graphene.